Loop-at-a-Time Stability Analysis for Grid-Connected Voltage-Source Converters

Zhang, Hongyang; Harnefors, Lennart; Wang, Xiongfei; Hasler, Jean-Philippe; Ostlund, Stefan; Danielsson, Christer; Gong, Hong

Published in:
IEEE Journal of Emerging and Selected Topics in Power Electronics

DOI (link to publication from Publisher):
10.1109/JESTPE.2020.3024103

Publication date:
2021

Document Version
Accepted author manuscript, peer reviewed version

Loop-at-a-Time Stability Analysis for Grid-Connected Voltage-Source Converters

Hongyang Zhang, *Student Member, IEEE,* Lennart Harnefors, *Fellow, IEEE,* Xiongfei Wang, *Senior Member, IEEE,* Jean-Philippe Hasler, Stefan Östlund, *Senior Member, IEEE,* Christer Danielsson, and Hong Gong, *Student Member, IEEE*

***Abstract*—The instability phenomena caused by converter–grid interactions can be prevented by designing controllers with adequate stability margins. Yet, the multiple-input multiple-output (MIMO) dynamics of grid-connected voltage-source converters (VSCs) complicate the stability analysis for the controller design. To tackle this challenge, this paper presents a loop-at-a-time stability analysis for grid-connected VSCs, which not only shows close correlations with the generalized Nyquist criterion for MIMO systems, but also enables to quantify the stability margins of individual closed loops. Moreover, the interactions between the closed loops can be analyzed. Test cases with numerical sensitivity analysis, simulations, and field measurements of a converter validate the theory.**

***Index Terms*—Multiple-input multiple-output (MIMO), loop-at-a-time (LAAT), generalized Nyquist stability criterion (GNC), single-input single-output (SISO), grid-connected voltage-source converters (VSCs).**

I. Introduction

INSTABILITY of a grid-connected voltage-source converter (VSC) can be caused by a weak-grid connection and/or be induced by poorly damped resonances in the grid [1]–[4]. The phenomena, and causes of instability, as well as the solutions for preventing instability, in the converter–grid interaction have been researched intensively [5]–[10].

In single-input single-output (SISO) dynamic systems, stability margins are clearly defined by evaluating the open-loop transfer function l (return ratio) [11], giving insights into the control design. Unfortunately, the closed-loop control of a grid-connected VSC is multiple-input multiple-output (MIMO). The stability of a MIMO system is usually checked by the generalized Nyquist stability criterion (GNC) with the determinant of $I + L$ (return difference) [12], where L is generalized to an open-loop transfer matrix[1]. However, this GNC-based analysis offers few insights into the control design, since the stability margins for $\det(I + L)$ are not as easily defined as for the SISO l [13], [14]. The characteristic loci for the eigenvalues λ_i of L[2] partially generalize the SISO Nyquist to MIMO systems [12], [15], [16]. However, such generalization is not strict, since stability margins on λ_i do not have the same implication as the SISO system.

Another possible approach to converter control design would be to adopt general MIMO design methods, such as H_2 or H_∞ control [17], where the controllers are synthesized by solving optimization problems. Alternatively, decentralized control with independent [18] or sequential loop closure [19] design could be considered. After the design, robustness analysis, e.g., μ analysis [20], evaluates the resulting controller. Such methods have been proven useful in process control.

Compared to the MIMO process control which may contain hundreds of inputs and outputs [21], the control of power electronic converters has a restricted structure. The open-loop plant has merely two input and output signals, i.e., the d and q components of the converter voltage reference and the converter current. Similar to the control of ac motor drives [22], the control structure of a grid-connected VSC is based on the principle of cascade control. The inner control loop contains current control (CC) function. The outer control loops include phase-locked loop (PLL), dc-bus voltage control (DVC), and ac-bus voltage control (AVC) functions. Thus, there are four nested control loops, but normally only the AVC has an external references. (All other references are generated internally within the control system.)

Compared to the MIMO control theory, the SISO method [21], [23] enables stability analysis for the design of the individual closed loops. When a time-domain specification is applied on specific control signals, the SISO method is convenient to check the design for that associated closed loop. In [24], SISO open-loop transfer functions are derived to design the DVC with the desired stability margins for the DVC loop.

Evaluating stability margins sequentially for MIMO systems are called loop-at-a-time (LAAT) analysis [21], [25]–[27]. Its principle is based on breaking each control loop at a time and make an evaluation for that broken loop. The LAAT analysis is essentially different from the sequential loop closure design [19]. With the latter approach, each control loop is closed sequentially and the controller in that closed loop is designed accordingly by shaping the closed-loop transfer functions. When one loop is closed for the design, the controllers in the other loops are not considered. On the other hand, the LAAT

H. Zhang, C. Danielsson and J. Hasler are with HITACHI ABB Power Grids, 72164, Västerås, Sweden (e-mail: hongyang.zhang@hitachi-powergrids.com, christer.danielsson@hitachi-powergrids.com, and jean-philippe.hasler@hitachi-powergrids.com).

L. Harnefors is with ABB, Corporate Research, 72178, Västerås, Sweden (e-mail: lennart.harnefors@se.abb.com). H. Zhang, L. Harnefors, X. Wang, and S. Östlund are with KTH Royal Institute of Technology, 10044, Stockholm, Sweden (email: stefano@kth.se).

X. Wang and H. Gong are with the Department of Energy Technology, Aalborg University, 9220 Aalborg East, Denmark (e-mail: xwa@et.aau.dk, hgo@et.aau.dk).

[1]To differentiate the return ratio l for a SISO, the return ratio for a MIMO is denoted as L.

[2]Characteristic loci are a variant of the GNC, since $\det(I+L) = 1+\prod_i \lambda_i$.

analysis ensures that all controllers are considered when a loop is broken.

In this paper, a framework for the LAAT stability analysis is presented for the grid-connected VSC. The control functions and main circuits are, in Section II, modeled as transfer matrices to construct a linearized MIMO closed-loop model. In Section III, a LAAT transfer matrix is derived with the forward and cross-coupling transfer functions and the LAAT stability analysis is introduced to evaluate the control design. Compared to [24], the LAAT stability analysis using this new model can be more intuitive, allowing two Nyquist curves to be plotted, for both the DVC and AVC loops, respectively. Further, In [24], only a SISO open-loop transfer function is derived by closing the DVC as the outest loop, where the AVC loop is embedded in the DVC-based SISO open-loop transfer functions. It is shown that, the LAAT stability analysis has close correlations with characteristic loci in the GNC. Moreover, it allows identifying stability margins of the individual closed loops, i.e., the DVC and AVC loops. In addition, the non-diagonal elements of the LAAT transfer matrix can be used for analyzing interactions between the closed loops. In Section IV, numerical sensitivity analyses, with various grid strength and control parameters, are shown to verify the effectiveness of the method. In Section V, measurement results from a high-power static synchronous compensator (STATCOM) installation are presented to validate the theory. In the end, Section VII summarizes the adopted controller design methods.

II. Small-Signal Modeling of the Grid-Connected VSC

A. Notation

In the stationary ($\alpha\beta$) reference frame and the synchronous (dq) reference frame, the elements are denoted with subscripts α and β or d and q respectively for the corresponding axes. The signals in the $\alpha\beta$ frame are denoted with a superscript 's', signals in the dq frame without a superscript. Note that lower-case letters are used for both vector and scalar variables. The latter are denoted with special subscripts, e.g., α, β, d, q, dc, acref, dcref. The subscripts with letters 'c', 'r', 't', 'p', and 'g' refer to 'converter', 'reactor', 'transformer', 'primary'[3], and 'grid', respectively. For instance, the converter current vectors in the $\alpha\beta$ and dq frame are denoted respectively as $i_c^s = [i_{c\alpha}^s, i_{c\beta}^s]^T$ and $i_c = [i_{cd}, i_{cq}]^T$, where i_c^s and i_c are column vectors, $i_{c\alpha}^s$, $i_{c\beta}^s$, i_{cd}, and i_{cq} are their corresponding scalar variables.

To represent perturbations, a prefix Δ is used, e.g., Δi_c. A constant representing a steady-state operating point contains a '0' in the end of its subscript, e.g., i_{c0}. As shown in [8], the dynamic impact of the PLL output can be calculated by introducing a so-called converter dq frame. In the converter dq frame, a superscript 'c' is added for distinction from the grid dq frame (which is the ordinary dq frame with no PLL impact), e.g., Δi_c^c.

[3]Primary refers to the bus on the primary side of the power transformer.

For simplicity, the Laplace variable s is omitted, e.g., G is short for $G(s)$. Transfer matrices and their elements are denoted as upper-case and lower-case letters, respectively, e.g.,

$$G = \begin{bmatrix} g_{11} & g_{12} \\ g_{21} & g_{22} \end{bmatrix}. \tag{1}$$

B. System Description

The basic circuit and control block diagrams of a three-phase grid-connected VSC are shown in Fig. 1. On the right-hand side of the VSC, the three-phase ac circuit is modeled in the $\alpha\beta$ frame. Phase reactors and a power transformer (if such is used) are located in series between the converter terminal and primary bus. The converter bus is on the right-hand side of of the phase reactors. The primary bus is connected to an infinite bus via a grid impedance. The transfer matrices for the phase reactors, power transformer and grid impedance are denoted as Z_r^s, Z_t^s, and Z_g^s, respectively, e.g.,

$$Z_r^s = \begin{bmatrix} R_r + sL_r & 0 \\ 0 & R_r + sL_r \end{bmatrix} \tag{2}$$

where R_r and L_r are the resistance and inductance of the phase reactor, respectively.

On the left-hand side of the VSC, the dc bus is modeled as a pure capacitor. The measurement and computation delays in the digital control system, along with the effect from the pulse-width modulation (PWM), have impacts on the high-frequency characteristics of the system [6] and they are omitted in this study. Since the PWM is omitted, an average model[4] is used. The model is generic for modeling of a modular multilevel converter (MMC) as a two-level converter (as shown in Fig. 1), as long as the MMC output voltage not affected by its internal dynamics [28] with proper modulation techniques [29]. The control system operates in the dq frame. The dq-frame correspondence of Z_r^s, Z_t^s, and Z_g^s are obtained by substituting $s \to s + j\omega_1$ [30], e.g.,

$$Z_r = Z_r^s + J\omega_1 L_r = \begin{bmatrix} R_r + sL_r & -\omega_1 L_r \\ \omega_1 L_r & R_r + sL_r \end{bmatrix} \tag{3}$$

where $J = \begin{bmatrix} 0 & -1 \\ 1 & 0 \end{bmatrix}$ and ω_1 is the angular grid frequency.

C. Controller Description

The basic control functions of the grid-connected VSC comprise the CC, PLL, DVC, and AVC (Fig. 1). Explicit descriptions of input-output relations of these functions in Fig. 1 are presented in Fig. 2.

1) PLL: The synchronous reference frame PLL [31] with a proportional integral (PI) regulator f_{PLL} is used so that the PLL output θ tracks the phase angle of u_c^s (see Fig. 2). A low-pass filter (LPF) h_{PLL} with the time constant τ_{PLL} is used to connect with the output of f_{PLL}, in order to filter out harmonic contents (mainly for the 2nd harmonic in the dq frame)

$$f_{\mathrm{PLL}} = k_{\mathrm{pPLL}}\left(1 + \frac{k_{\mathrm{iPLL}}}{s}\right), \quad h_{\mathrm{PLL}} = \frac{1}{1 + s\tau_{\mathrm{PLL}}}. \tag{4}$$

[4]The relation between the ac and dc side of the converter is based on the principle of power balancing.

This article has been accepted for publication in a future issue of this journal, but has not been fully edited. Content may change prior to final publication. Citation information: DOI 10.1109/JESTPE.2020.3024103, IEEE Journal of Emerging and Selected Topics in Power Electronics

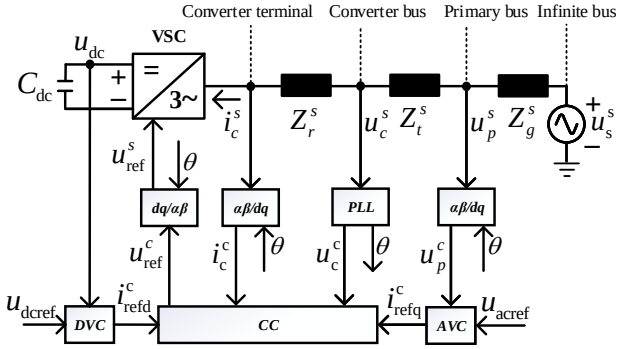

Fig. 1. Basic circuit and control block diagrams of the grid-connected VSC.

2) CC: Since the CC is implemented in the dq frame, thus a PI regulator $f_{\rm CC}$ is used. For removal of harmonics and improvement of stability [8], LPFs $h_{\rm uFF}$ with the time constant $\tau_{\rm uFF}$ is used to feedforward both $u^c_{\rm cd}$ and $u^c_{\rm cq}$ into the CC

$$f_{\rm CC} = k_{\rm pCC}\left(1+\frac{k_{\rm iCC}}{s}\right), \quad h_{\rm uFF} = \frac{1}{1+s\tau_{\rm uFF}}. \tag{5}$$

The dq-axes current reference vector $i^{\rm c}_{\rm ref}$ is connected through a transfer matrix $H_{\rm iFF}$ (as a feedforward function), for improving dynamic performance [32]

$$H_{\rm iFF} = \begin{bmatrix} \frac{s}{1+s\tau_{\rm iFF}} & -\omega_1 \\ \omega_1 & \frac{s}{1+s\tau_{\rm iFF}} \end{bmatrix} L_r \tag{6}$$

where $\tau_{\rm iFF}$ is the time constant for the lead filter, and the off-diagonal elements of $H_{\rm iFF}$ represent the cross-couplings between the dq axes.

3) DVC: The harmonic ripples of the dc-bus voltage $u_{\rm dc}$ are filtered via a LPF $h_{\rm DVC}$ with the time constant $\tau_{\rm DVC}$, i.e., $u_{\rm dcf} = h_{\rm DVC}u_{\rm dc}$. The DVC error $e_{\rm DVC} = u_{\rm dcref} - u_{\rm dcf}$ ($u_{\rm dcref}$ is the dc-bus voltage reference) is controlled by a PI regulator $f_{\rm DVC}$

$$f_{\rm DVC} = k_{\rm pDVC}\left(1+\frac{k_{\rm iDVC}}{s}\right), \quad h_{\rm DVC} = \frac{1}{1+s\tau_{\rm DVC}}. \tag{7}$$

4) AVC: The d-component of $u^c_{\rm p}$ is filtered with a LPF $h_{\rm AVC}$ which yields $u^c_{\rm pdf}$. The AVC regulator $f_{\rm AVC}$ minimizes the AVC error $e_{\rm AVC} = u_{\rm acref} - u^c_{\rm pdf}$, where $u_{\rm acref}$ is the ac-bus voltage reference. Finally, $f_{\rm AVC}$ contains only a pure integrator function

$$f_{\rm AVC} = \frac{k_{\rm iAVC}}{s}, \quad h_{\rm AVC} = \frac{1}{1+s\tau_{\rm AVC}}. \tag{8}$$

D. MIMO Small-Signal Modeling

In this section, a MIMO small-signal modeling procedure is presented for the grid-connected VSC. The detailed derivation of the small-signal model can be found in the Section VII.

1) Inner Closed Loop: The inner closed loop is composed of the transfer matrices of the CC, PLL and its related dynamics, and passive circuit elements. PLL is often categorized as an outer closed loop [6], due to its similar closed-loop bandwidth to those of the DVC and the AVC loops. In this paper, since the PLL mostly impacts the inner loop, thus the PLL is categorized as the inner closed loop. The schematic of the linearized inner closed loop is illustrated in Fig. 3. (phase reactor admittance $Y_r(=Z_r{}^{-1})$, sum of the grid and transformer impedance Z_{gt} $(=Z_g+Z_t)$ are illustrated.) For the infinite bus, we have $\Delta u_s = 0$.

The closed-loop transfer matrix T_i (from $\Delta i^c_{\rm ref}$ to $\Delta i_{\rm c}$) is derived as

$$T_i = G^{-1}_{\rm i2}G^{-1}_{\rm i1}Y_r(F_{\rm CC}+H_{\rm iFF}) \tag{9}$$

where $G_{\rm i1} = I_2 + Y_rZ_{\rm gt} - Y_r(H_{\rm uFF}G_{\rm PLL1}+G_{\rm PLL3})Z_{\rm gt}$, $G_{\rm i2} = I_2 + G^{-1}_{\rm i1}Y_rF_{\rm CC}(I_2 - G_{\rm PLL2}Z_{\rm gt})$ [see (21) to (28) in Section VII for detailed derivations].

Note that to construct the outer closed loops in Fig. 3, $\Delta i_{\rm c}$ is selected, instead of $\Delta i^c_{\rm c}$, as the output of T_i, such that the voltages of the outer loops $\Delta u_{\rm o}$ can be computed with $\Delta i_{\rm c}$ on the same dq frame. In the end, the impact of the PLL is included to convert $\Delta u_{\rm o}$ to $\Delta u^c_{\rm o}$, see Section II-D2. In addition, the unity feedback closed-loop transfer matrix $T_{\rm iUF}$ (from $\Delta i^c_{\rm ref}$ to $\Delta i^c_{\rm c}$) is derived as

$$T_{\rm iUF} = G^{-1}_{\rm i2UF}(I_2 - G_{\rm PLL2}Z_{\rm gt})G^{-1}_{\rm i1}Y_r(F_{\rm CC}+H_{\rm iFF}) \tag{10}$$

where $G_{\rm i2UF} = I_2 + (I_2 - G_{\rm PLL2}Z_{\rm gt})G^{-1}_{\rm i1}Y_rF_{\rm CC}$.

2) Outer Closed Loop: The outer loops use unity negative feedbacks and they are closed by the outer-loop controllers, written as a transfer matrix F_o in Fig. 3. A transfer matrix G_o is defined for input $\Delta i_{\rm c}$ and output $\Delta u^c_{\rm o}$

$$F_o = \begin{bmatrix} f_{\rm DVC} & 0 \\ 0 & f_{\rm AVC} \end{bmatrix}, \quad G_o = \begin{bmatrix} g_{o11} & g_{o12} \\ g_{o21} & g_{o22} \end{bmatrix}. \tag{11}$$

The function of G_o is for voltage calculation and filtering for the feedbacks from the DVC ($\Delta u_{\rm dcf}$) and the AVC ($\Delta u^c_{\rm pdf}$) loops. F_o is designed to have $\Delta u^c_{\rm o} = [\Delta u_{\rm dcf}, \Delta u^c_{\rm pdf}]^T$ track $\Delta u_{\rm ref} = [\Delta u_{\rm dcref}, \Delta u_{\rm acref}]^T$.

We defined that $G_o = [G_{\rm o1}, G_{\rm o2}]^T$ [see (29) to (34) in Section VII for detailed expressions], where $G_{\rm o1}$ and $G_{\rm o2}$ represent the voltage calculation and filtering process for the DVC and AVC, respectively. An equivalent schematic of Fig. 3 is shown in Fig. 4 (a), where $G = G_oT_i$ is the open-loop plant on which F_o is acting. Note that G contains the dynamics of CC, PLL, and passive components. G also has the feature that operating points are embedded. Cascading G and F_o forms the open-loop transfer matrix $L = GF_o$. In turn, the closed-loop transfer matrix (from $\Delta u_{\rm ref}$ to $\Delta u^c_{\rm o}$) is obtained as

$$T = (I_2 + L)^{-1}L. \tag{12}$$

The elements of L and T are respectively expressed as

$$L = \begin{bmatrix} l_{11} & l_{12} \\ l_{21} & l_{22} \end{bmatrix}, \quad T = \begin{bmatrix} t_{11} & t_{12} \\ t_{21} & t_{22} \end{bmatrix}, \tag{13}$$

to be used in the sequel.

III. LAAT Stability Analysis

In Section III, LAAT stability analysis is introduced for analyzing the stability of generic MIMO models alike which is introduced in Section II.

This article has been accepted for publication in a future issue of this journal, but has not been fully edited. Content may change prior to final publication. Citation information: DOI 10.1109/JESTPE.2020.3024103, IEEE Journal of Emerging and Selected Topics in Power Electronics

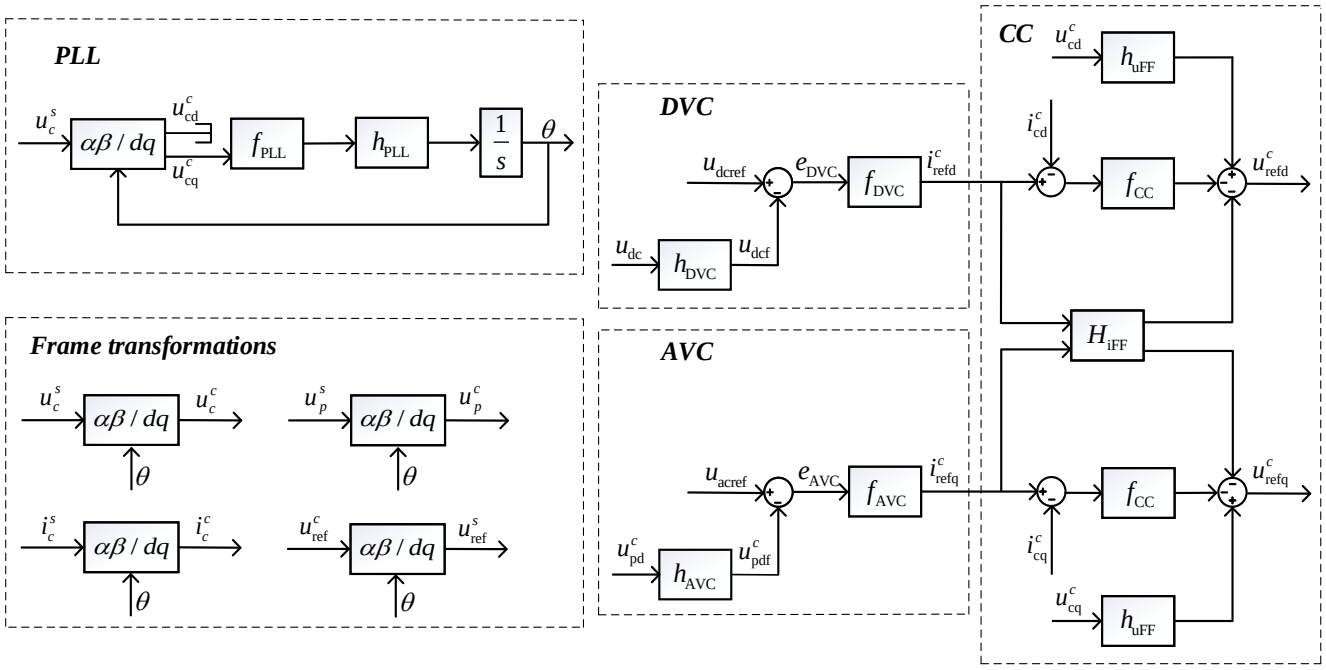

Fig. 2. Explicit descriptions of input-output relations of control functions in Fig. 1.

A. LAAT Transfer Matrix

An equivalent schematic of the DVC and AVC loops, with expressions of elements l_{11}, l_{12}, l_{21}, and l_{22} in L is shown in Fig. 4 (b). Note that both l_{11} and l_{22} can be named as forward transfer functions [33], without cross couplings for the DVC and AVC loops, respectively. Correspondingly, l_{12} and l_{21} are denoted as the cross-coupling transfer functions. Based on this structure, the LAAT stability analysis can be done by introducing the modified open-loop transfer matrix L_{LAAT} as

$$L_{\mathrm{LAAT}} = \begin{bmatrix} l_{\mathrm{LAAT11}} & l_{\mathrm{LAAT12}} \\ l_{\mathrm{LAAT21}} & l_{\mathrm{LAAT22}} \end{bmatrix}, \tag{14}$$

which can be derived so that l_{LAAT11}, l_{LAAT12}, l_{LAAT21}, and l_{LAAT22} are the respective open-loop transfer functions for t_{11}, t_{12}, t_{21}, and t_{22}, e.g., $t_{11} = l_{\mathrm{LAAT11}}/(1 + l_{\mathrm{LAAT11}})$

$$L_{\mathrm{LAAT}} = \begin{bmatrix} t_{11}/(1-t_{11}) & t_{12}/(1-t_{12}) \\ t_{21}/(1-t_{21}) & t_{22}/(1-t_{22}) \end{bmatrix}. \tag{15}$$

The rationale of the diagonal elements of L_{LAAT} is that they are the open-loop transfer functions for breaking one loop while having the other loop closed. For instance, for a 2×2 system, K is defined as the loop transfer matrix $K = \mathrm{diag}(k_1, k_2)$, where k_i $(i = 1, 2)$ determines which loops are closed or broken [see Fig. 4(b)]. Let us define L_1 which yields

$$L_1 = (I_2 + LK)^{-1} L. \tag{16}$$

The following results can be concluded:

- $K = 0_2$. All loops are broken.
- $K = \mathrm{diag}(0, 1)$. The first loop is broken and the second loop is closed.
- $K = \mathrm{diag}(1, 0)$. The second loop is broken and the first loop is closed.

Therefore, by breaking one of the two feedback loops, a SISO open-loop transfer function can always be obtained from a 2×2 MIMO. It can be shown that $L_{\mathrm{LAAT}}(1,1) = L_1(1,1)$, with $K = \mathrm{diag}(0, 1)$ and $L_{\mathrm{LAAT}}(2,2) = L_1(2,2)$, with $K = \mathrm{diag}(1, 0)$. By evaluating the diagonal parts of L_{LAAT}, the classical SISO stability margins can be obtained for the corresponding diagonal elements of T. Furthermore, we can use the off-diagonal elements in L_{LAAT} to check the interaction effects between the loops. The same principle of a 2×2 L_{LAAT} matrix can be applied to a $n \times n$ matrix for $n \times n$ MIMO in general.

Using (12), the elements in T can be represented by the elements (l_{11}, l_{12}, l_{21}, and l_{22}) in L, which yields

$$T = \frac{1}{\det(I + L)} \begin{bmatrix} l_{11} + l_{11}l_{22} - l_{12}l_{12} & l_{12} \\ l_{21} & l_{22} + l_{11}l_{22} - l_{21}l_{12} \end{bmatrix}. \tag{17}$$

The explicit form of L_{LAAT} can also be obtained as

$$L_{\mathrm{LAAT}} = \begin{bmatrix} l_{11} - l_{12}l_{21}/(1 + l_{22}) & l_{12}/[\det(I_2 + L) - l_{12}] \\ l_{21}/[\det(I_2 + L) - l_{21}] & l_{22} - l_{21}l_{12}/(1 + l_{11}) \end{bmatrix}. \tag{18}$$

In (18), each element in L_{LAAT} is derived so that it contains all the elements (l_{11}, l_{12}, l_{21}, and l_{22}) in L. This gives an intuitive sense how L_{LAAT} can be used for evaluation, since the impacts from individual forward (l_{11}, l_{22}) and cross-coupling (l_{12}, l_{21}) transfer functions can be analyzed independently.

B. Evaluation of Stability

Note that in each element of L_{LAAT} in (18), there exists an internal closed diagonal loop. For instance, the forward

This article has been accepted for publication in a future issue of this journal, but has not been fully edited. Content may change prior to final publication. Citation information: DOI 10.1109/JESTPE.2020.3024103, IEEE Journal of Emerging and Selected Topics in Power Electronics

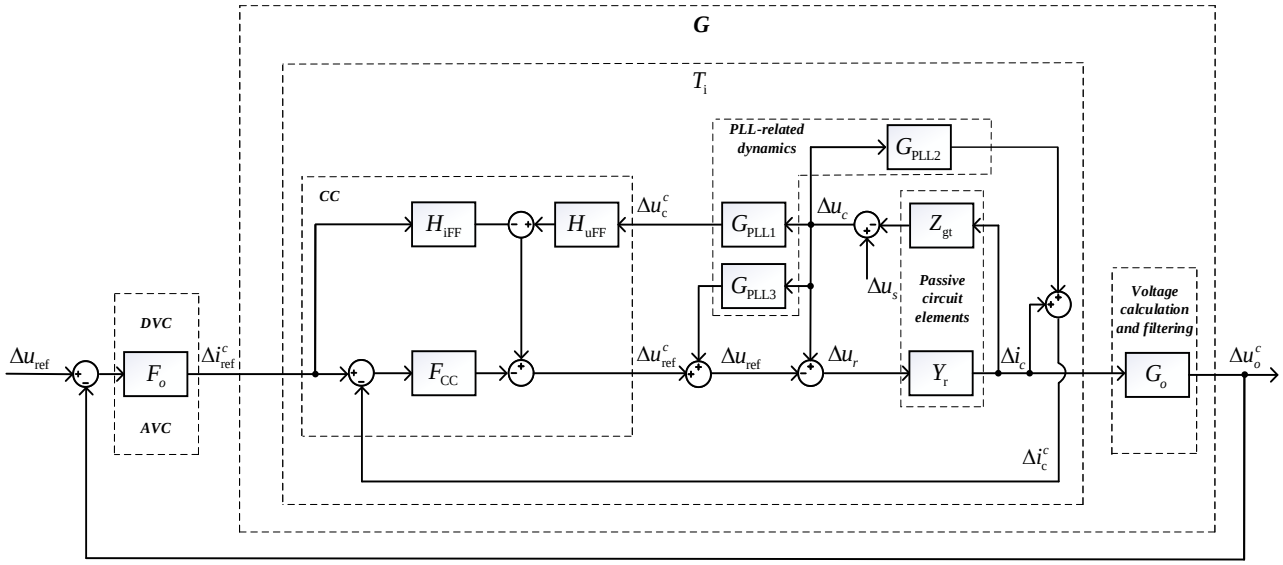

Fig. 3. Schematic of the linearized MIMO closed-loop control blocks for the inner and outer loops.

transfer function l_{22} for the AVC loop (Fig. 4) is embedded in the denominator within l_{LAAT11} for the DVC loop. This implies a special condition on evaluating L_{LAAT} in the frequency domain[5]: when evaluating the diagonal elements l_{LAAT11} or l_{LAAT22}, the Nyquist plots of l_{22} or l_{11} (both are actually Nyquist arrays) must not encircle $-1+j0$. In [24], it is shown that for the DVC closed loop, in total three Nyquist curves need to be evaluated for the design and none of them should encircle $-1+j0$. In this paper we generalize and simplify the method such that there is only one embedded closed loop, and only two Nyquist curves are checked for each loop. For instance, for the AVC loop, we evaluate l_{LAAT22} and l_{11}.

It is reasonable to assume that T_i is stable. Exceptions are when k_{iCC} or F_{PLL} are designed aggressively [8][6]. We also know that F_o contains only casual transfer functions, and G_o is a stable transfer function matrix. Therefore L is stable. It is worth noting that L is assumed to be internally stable (no right-half-plane pole-zero cancellations). Then it is straightforward to check whether l_{11} and l_{22} encirle $-1+j0$. The system is usually treated as a SISO, when designing the current control loop [8], [30], [34]. For evaluating the stability of the inner closed loops, the LAAT analysis can also be used to check the stability margins. The unity feedback closed-loop T_{iUF} can then be broken at its feedback Δi_c^c. Therefore, L_{LAAT} for the inner closed loop can be derived by cascading transfer matrices from $\Delta i_{\mathrm{ref}}^c$ to Δi_c^c. Since the primary purpose of this paper is to introduce the LAAT method with a focus on the stability analysis of the outer closed loops, using the LAAT stability analysis for the inner closed-loop is not discussed further. It is assumed that the inner closed loops are always stable.

[5]Alike omitting s for transfer functions, $j\omega$ is also omitted for frequency responses.

[6]This refers that a large value of k_{iCC}, k_{pPLL}, or k_{iPLL} could lead to the instability. Also, T_i can also be unstable when it contains large time delays [6].

TABLE I
TEST-SYSTEM DATA AND DEFAULT CONTROLLER PARAMETERS.

Symbol	Value	Definition
U_{base}	28.17 kV	Base voltage, peak value space-vector scaling
I_{base}	2.37 kA	Base current, peak value space-vector scaling
Z_{base}	11.9 Ω	Base impedance
C_{dc}	1.0 mF	DC-bus capacitance
X_{r}	0.10 p.u.	Phase-reactor inductance
X_{t}	0.10 p.u.	Transformer inductance
X_{gmin}	0.2 p.u.	Minimum grid reactance
X_{gmax}	0.5 p.u.	Maximum grid reactance
ω_1	100π rad/s	Nominal angular frequency
u_{dcref}	1.4 p.u.	DC-bus voltage reference
u_{acref}	1.1 p.u.	AC-bus voltage reference
τ_{rAVC}	100 ms	AVC step response required rise time

TABLE II
DEFAULT CONTROLLER PARAMETERS.

Symbol	Value	Definition
ω_{s}	20000π rad/s	Sampling frequency
τ_{vFF}	1.0 ms	CC voltage feedforward time constant
τ_{iFF}	1.0 ms	CC lead filter time constant
τ_{PLL}	10 ms	PLL LPF time constant
τ_{DVC}	10 ms	DVC LPF time constant
τ_{AVC}	5.0 ms	AVC LPF time constant

C. Comparison With the GNC

Considering an internal stable L, the evaluation of the closed-loop stability with either LAAT analysis or characteristic loci of L should guarantee no encirclement of $-1+j0$. As discussed in Section III-A, the gain and phase margins for l_{LAAT11}, l_{LAAT22} indicate the classical SISO margins for each individual loops. On the other hand, the stability margins seen from λ_1, λ_2 in GNC are not equivalent to the classical SISO margins.

Suppose L and T can be decomposed as

$$L = W\Lambda_L W^{-1}, \quad T = W\Lambda_T W^{-1} \tag{19}$$

This article has been accepted for publication in a future issue of this journal, but has not been fully edited. Content may change prior to final publication. Citation information: DOI 10.1109/JESTPE.2020.3024103, IEEE Journal of Emerging and Selected Topics in Power Electronics

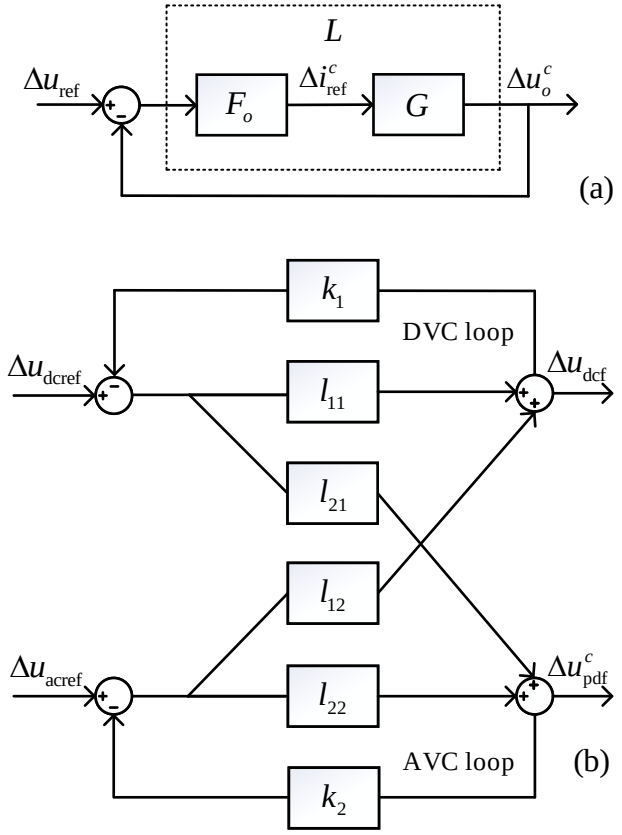

Fig. 4. (a) Schematic of the equivalent MIMO system to Fig. 3. (b) Schematic of the DVC and AVC loops, expressed with l_{11}, l_{12}, l_{21}, and l_{22} in L.

TABLE III
DESIGNED CONTROLLER PARAMETERS.

Symbol	Value	Definition
k_{pCC}	1.0 p.u.	CC proportional gain
k_{iCC}	10.0 rad/s	CC integral gain
k_{pPLL}	30.0 rad/s	PLL proportional gain
k_{iPLL}	1.0 rad/s	PLL integral gain
k_{pDVC}	1.2 p.u.	DVC proportional gain
k_{iDVC}	10.0 rad/s	DVC integral gain
k_{iAVC}	110 rad/s	AVC integral gain

where $\Lambda_L = \mathrm{diag}\{\lambda_1, \lambda_2\}$ and the columns of W are the right eigenvectors of L, $\Lambda_T = [I + \Lambda_L]^{-1}\Lambda_L = \mathrm{diag}\{\lambda_1/[1+\lambda_1], \lambda_2/[1+\lambda_2]\}$. Then L and Λ_L are similar as well for T and Λ_T, evaluating of λ_1 and λ_2 for the individual loops is equivalent to checking L as for SISO if $W = I_2$. In other words, unless L is a diagonal matrix – for a diagonal L, checking $\lambda_1 = l_{11}$ and $\lambda_2 = l_{22}$ is equivalent to the classical SISO margins.

Solving the roots for $\det(\lambda I - L)$ yields

$$\lambda_{1,2} = \frac{l_{11} + l_{22} \pm \sqrt{(l_{11} - l_{22})^2 + 4 l_{12} l_{21}}}{2}. \qquad (20)$$

If l_{12} and l_{21} are relatively small (which indicates that the MIMO is weakly interacted), L is closed to a diagonal matrix. Checking $\lambda_{1,2}$ is then almost equivalent to the LAAT margins. Examples with strong MIMO interactions are listed in the Appendix VII.

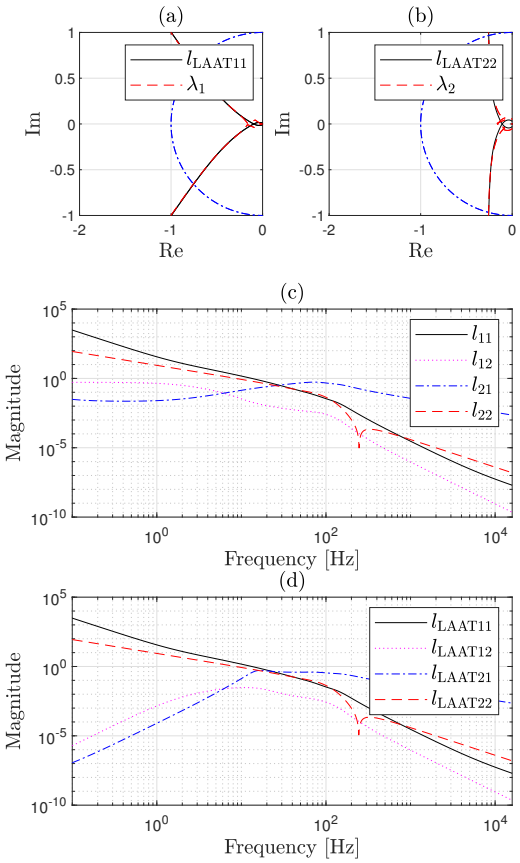

Fig. 5. (a) Nyquist plots for l_{LAAT11} and λ_1. (b) Nyquist plots for l_{LAAT22} and λ_2. (c) Bode magnitude plots of l_{11}, l_{12}, l_{21}, and l_{22}. (d) Bode magnitude plots of l_{LAAT11}, l_{LAAT12}, l_{LAAT21}, and l_{LAAT22}.

IV. Case Study

This section presents case studies with numerical sensitivity analysis to illustrate the effectiveness of the LAAT stability analysis are presented. The control structures as well as the modeling introduced in Section in II are implemented.

A. Test System

A 100-MVA STATCOM is connected to a 34.5-kV bus in an inductive grid with short circuit ratio (SCR) = 2 (SCR = $1/X_{\mathrm{g}}$, where $X_{\mathrm{g}} = Z_{\mathrm{g}}$). The basic circuit parameters and reference values are shown in Table I. The default STATCOM controller parameters are listed II. In a practical STATCOM control system, u_{dcref} is kept constant during the operation. The typical requirement for a STATCOM is usually specified by a step-response on u_{acref} [35]. Having the setpoint value of $u_{\mathrm{acref}} = 1.1$ per unit (p.u.) with $u_{\mathrm{sd0}} = 1.0$ p.u., the maximum capacitive current yields $i_{\mathrm{cq0}} = 0.2$ p.u., which is the operating point for the design. We assume that $R_r = R_t = R_g = 0.001$ p.u. and that the converter is lossless. The controller parameters are tuned based on the design procedures described in Appendix VII, and their values are shown in Table III[7].

[7]Time is not normalized, leading to certain parameters having the dimension angular frequency.

This article has been accepted for publication in a future issue of this journal, but has not been fully edited. Content may change prior to final publication. Citation information: DOI 10.1109/JESTPE.2020.3024103, IEEE Journal of Emerging and Selected Topics in Power Electronics

In Section IV-H, case studies for a strong-grid condition are performed.

B. Stability Evaluations of the Design

Stability of the design is checked by the LAAT analysis. In Fig. 5 (a) and Fig. 5 (b) , the Nyquist plots of l_{LAAT11} and l_{LAAT22} are shown for the condition with SCR $= 2$. Stability margins for the DVC and AVC loops are respectively evaluated by l_{LAAT11} and l_{LAAT22}. We observe that none of the Nyquist curves encircles $-1 + j0$ and adequate stability margins are obtained for individual closed loops. Due to the fact that the DVC bandwidth is designed more aggressively than the AVC bandwidth (see Appendix VII), less phase margins are obtained for l_{LAAT22} compared to l_{LAAT11}.

C. Interaction Analysis

In Section III-A, it is shown that l_{LAAT12} and l_{LAAT21} in L_{LAAT} can be used to check the interaction effects between the loops. The Bode magnitude plots of l_{11}, l_{12}, l_{21}, and l_{22}, as well as l_{LAAT11}, l_{LAAT12}, l_{LAAT21}, and l_{LAAT22} are shown in Fig. 5 (c) and Fig. 5 (d), respectively. For frequencies higher than 50 Hz, we find relatively higher magnitude of l_{LAAT21}, which indicates strong interactions from $\Delta u_{\mathrm{dcref}}$ to $\Delta u^{c}_{\mathrm{pdf1}}$. On contrary, the magnitude of l_{LAAT12} remains low for all frequencies.

D. Comparison With the GNC

To verify the conclusions of Section III-C, Nyquist plots of l_{LAAT11} with λ_1, and l_{LAAT22} with λ_2 are shown in Fig. 5 (a) and Fig. 5 (b). Due to relatively small $l_{12}l_{21}\ \forall\ f$, see Fig. 5 (c), from (20) we have $\lambda_1 \approx l_{\mathrm{LAAT11}} \approx l_{11}$, and $\lambda_2 \approx l_{\mathrm{LAAT22}} \approx l_{22}$. The Nyquist plots of l_{LAAT11} with λ_1, and l_{LAAT22} with λ_2 are almost overlapping.

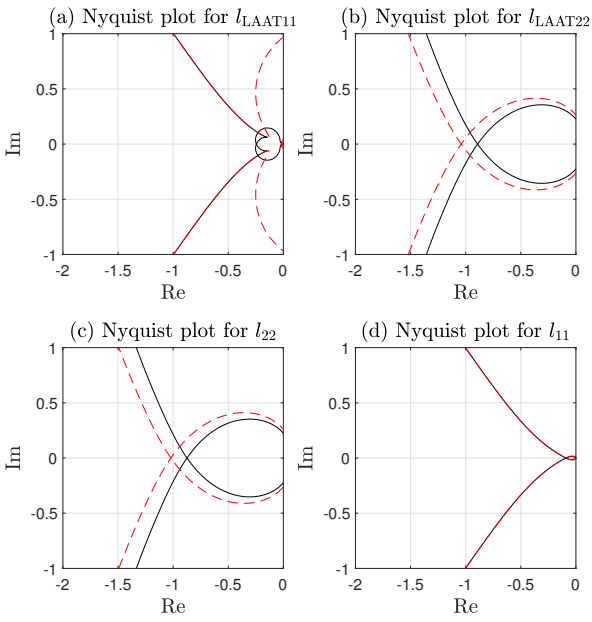

Fig. 7. Nyquist plots for l_{LAAT11}, l_{LAAT22}, l_{11}, and l_{22}. Black solid curve: $k_{\mathrm{iAVC}} = 900$ rad/s. Red dashed curve: $k_{\mathrm{iAVC}} = 1050$ rad/s.

E. Sensitivity Analysis With Grid Impedance Variations

As discussed in Section VII-D2, X_g could be of any values within $[X_{\mathrm{gmin}}, X_{\mathrm{gmax}}]$. Therefore, we evaluate l_{LAAT11} and l_{LAAT22} [see Fig. 6 (a) and Fig. 6 (f)] with SCR $= 2$ p.u., SCR $= 3.5$ p.u., and SCR $= 5$ p.u. We find that the stability

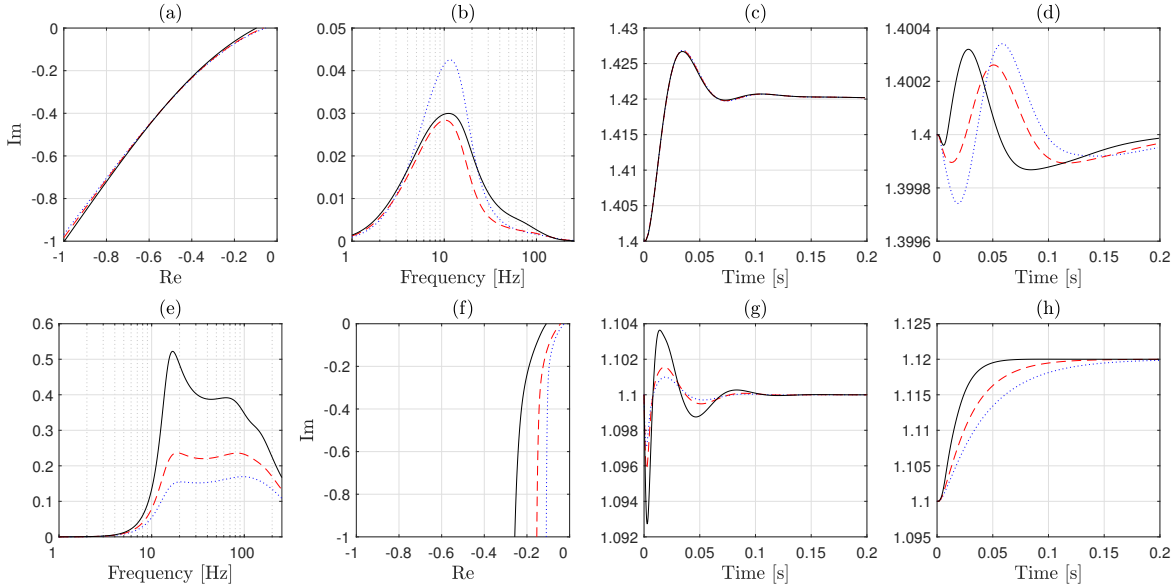

Fig. 6. Sensitivity and interaction analysis with grid impedance variations SCR $= 2$ p.u. (black solid curves), SCR $= 3.5$ p.u. (red dashed curves), and SCR $= 5$ p.u. (blue dotted curves). Frequency-domain results: (a) Nyquist plots for l_{LAAT11}. (b) Bode magnitude plots [p.u.] for l_{LAAT12}. (e) Bode magnitude plots [p.u.] for l_{LAAT21}. (f) Nyquist plots for l_{LAAT22}; Time-domain results: (c) Response for u_{dcf} [p.u.] with $\Delta u_{\mathrm{dcref}} = 0.02$ p.u. (d) Response for u_{dcf} [p.u.] with $\Delta u_{\mathrm{acref}} = 0.02$ p.u. (g) Response for u^{c}_{pdf} [p.u.] with $\Delta u_{\mathrm{dcref}} = 0.02$ p.u. (h) Response for u^{c}_{pdf} [p.u.] with $\Delta u_{\mathrm{acref}} = 0.02$ p.u.

This article has been accepted for publication in a future issue of this journal, but has not been fully edited. Content may change prior to final publication. Citation information: DOI 10.1109/JESTPE.2020.3024103, IEEE Journal of Emerging and Selected Topics in Power Electronics

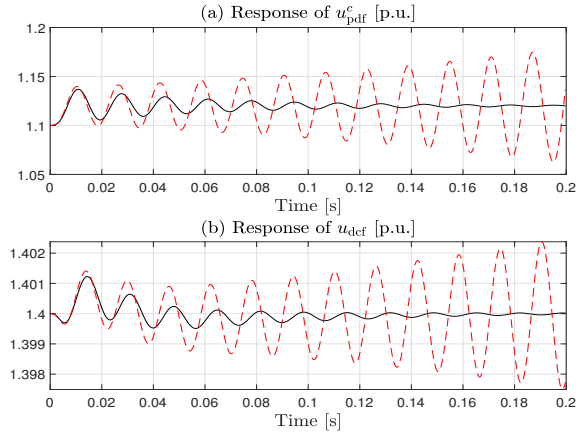

Fig. 8. Responses to a 0.02-p.u. step change of $u_{\rm acref}$. Black solid curve: $k_{\rm iAVC} = 900$ rad/s. Red dashed curve: $k_{\rm iAVC} = 1050$ rad/s.

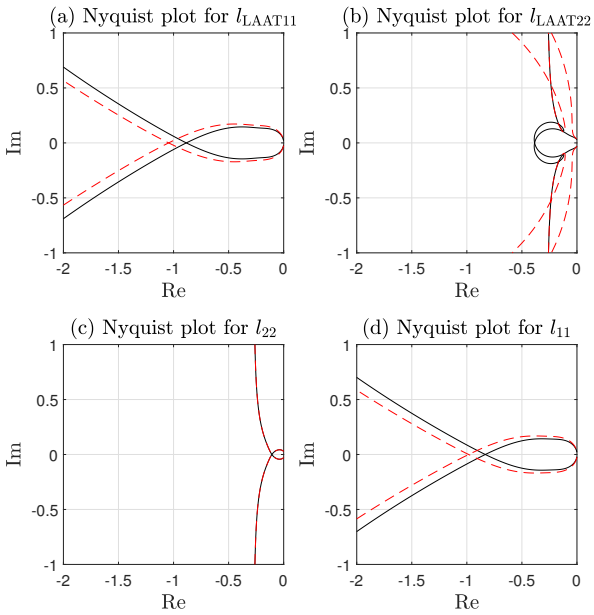

Fig. 9. Nyquist plots for $l_{\rm LAAT11}$, $l_{\rm LAAT22}$, l_{11}, and l_{22}. Black solid curve: $k_{\rm pDVC} = 11$ p.u. Red dashed curve: $k_{\rm pDVC} = 13$ p.u.

margins remain almost unchanged for $l_{\rm LAAT11}$ for all grid conditions (which also confirms the DVC design in Appendix VII-D1). From SCR = 2 p.u. to SCR = 5 p.u., both gain and phase margins gradually increase for $l_{\rm LAAT22}$, which shows robust design for both the DVC and AVC loops. A step-response test with $\Delta u_{\rm acref} = 0.02$ p.u. for $u^c_{\rm pdf}$ is shown in Fig. 6 (h) for all the SCR conditions. A requirement of $\tau_{\rm rAVC} = 100$ ms is therefore met. In addition, the response of $u_{\rm dcf}$ under $\Delta u_{\rm acref} = 0.02$ p.u. is shown in Fig. 6 (d). It is found $u_{\rm dcf}$ limited influenced by a step change on $u_{\rm acref}$. This is verified by Bode magnitude plots for $l_{\rm LAAT12}$ in Fig. 6 (b). Similarly, $\Delta u_{\rm dcref} = 0.02$ p.u. is applied and the response from $u_{\rm dcf}$ and $u^c_{\rm pdf}$ are shown in Fig. 6 (c) and Fig. 6 (g), respectively. It can be seen that the rise time for the DVC is designed faster than the AVC. Due to relative high interactions from $u_{\rm dcf}$ to $u^c_{\rm pdf}$ [see Fig. 6 (e)], $u^c_{\rm pdf}$ varies with relative

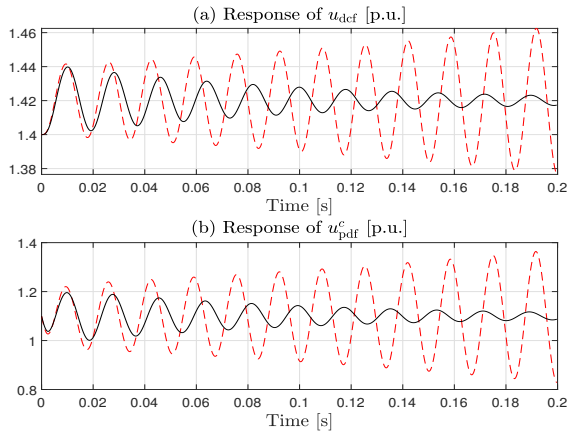

Fig. 10. Responses to a 0.02-p.u. step change of $u_{\rm dcref}$. Black solid curve: $k_{\rm pDVC} = 11$ p.u. Red dashed curve: $k_{\rm pDVC} = 13$ p.u.

larger magnitude. Also, the variations are greatly influenced by different SCR conditions, with stronger grid, the variations of $u^c_{\rm pdf}$ is to be smaller.

F. Stability Impacts With AVC Parameter Variations

1) Before Losing Stability: We increase $k_{\rm iAVC}$ to 900 rad/s to push the system close to the boundary of losing asymptotic stability. The Nyquist curves for $l_{\rm LAAT11}$ and $l_{\rm LAAT22}$ are found in Fig. 7 (a) and Fig. 7 (b) respectively. The AVC margin is now greatly reduced and the Nyquist curve of $l_{\rm LAAT22}$ and l_{22} [see Fig. 7 (c)] are closed to encircle $-1 + j0$. It may be read from Fig. 7 (b) that the gain margin (GM)= 1.12 p.u. at $\omega = 387$ rad/s and the phase margin (PM)= 8.82 deg at $\omega = 351$ rad/s. To verify this in the time-domain, a 0.02-p.u. step in $u_{\rm acref}$ is applied at Time= 2 s, giving the response shown in Fig. 8. Converging oscillations can be observed on $u^c_{\rm pdf}$ and $u_{\rm dcf}$.

2) Unstable: We further increase $k_{\rm iAVC}$ to 1050 rad/s (1.17 times of 900 rad/s, which is higher than the GM= 1.12 p.u. of the previous condition $k_{\rm iAVC} = 900$ rad/s) to push the system to be unstable. The red dashed Nyquist curves are found in Fig. 7. When system becomes unstable, both $l_{\rm LAAT22}$ and l_{22} [Fig. 7 (c)] encircle $-1 + j0$. It is found that $l_{\rm LAAT11}$ changes dramatically from the condition at $k_{\rm iAVC} = 900$ rad/s, when l_{22} encircles $-1 + j0$. The time-domain simulation shows an unstable closed-loop system, see Fig. 8.

G. Stability Impacts With DVC Parameter Variations

1) Before Losing Stability: We increase $k_{\rm pDVC}$ to 11 p.u. to push the system close to the boundary of losing asymptotic stability. The black solid Nyquist curves are in Fig. 9. The DVC margin is now small and the Nyquist curve of $l_{\rm LAAT11}$ and l_{11} [see Fig. 9 (d)] are closed to encircle $-1 + j0$. Seen from Fig. 9 (a) that the GM= 1.13 p.u. and the phase margin (PM)= 3.4 deg. To verify this in the time-domain, a 0.02-p.u. step in $u_{\rm dcref}$ is applied at Time= 2 s, giving the response shown in Fig. 10. Converging oscillations can be observed on $u_{\rm dcf}$ and $u^c_{\rm pdf}$.

This article has been accepted for publication in a future issue of this journal, but has not been fully edited. Content may change prior to final publication. Citation information: DOI 10.1109/JESTPE.2020.3024103, IEEE Journal of Emerging and Selected Topics in Power Electronics

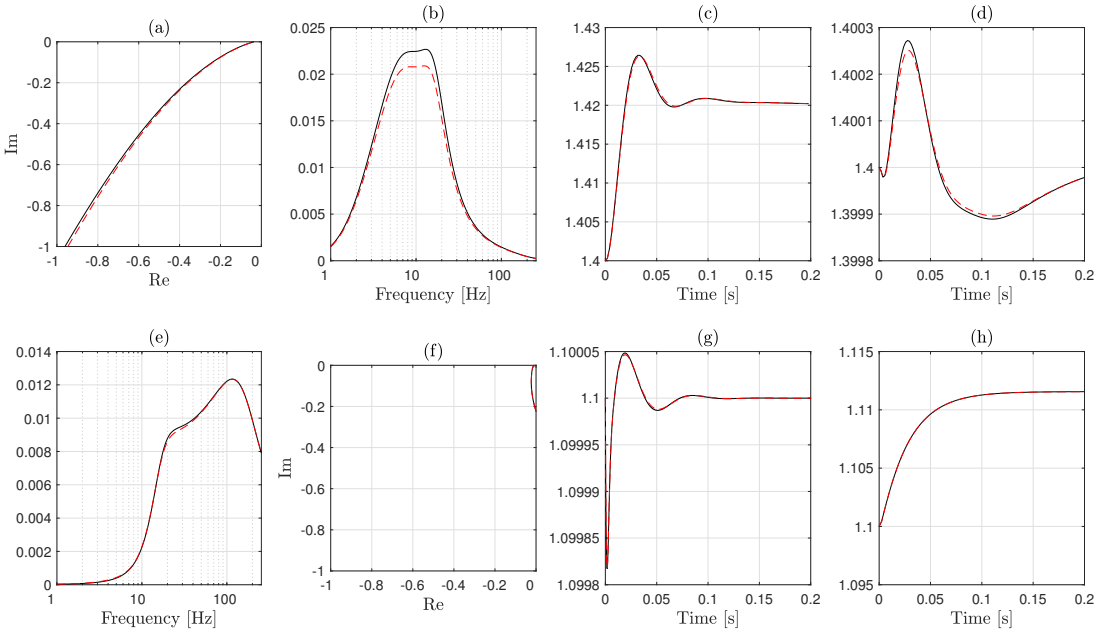

Fig. 11. Sensitivity and interaction analysis with grid impedance SCR $= 90$ p.u. for $i_{\mathrm{cq0}} = 0.2$ p.u. (black solid curves) and $i_{\mathrm{cq0}} = -0.2$ p.u. (red dashed curves). Frequency-domain results: (a) Nyquist plots for l_{LAAT11}. (b) Bode magnitude plots [p.u.] for l_{LAAT12}. (e) Bode magnitude plots [p.u.] for l_{LAAT21}. (f) Nyquist plots for l_{LAAT22}; Time-domain results: (c) Response for u_{dcf} [p.u.] with $\Delta u_{\mathrm{dcref}} = 0.02$ p.u. (d) Response for u_{dcf} [p.u.] with $\Delta u_{\mathrm{acref}} = 0.02$ p.u. (g) Response for u^c_{pdf} [p.u.] with $\Delta u_{\mathrm{dcref}} = 0.02$ p.u. (h) Response for u^c_{pdf} [p.u.] with $\Delta u_{\mathrm{acref}} = 0.02$ p.u.

2) Unstable: We increase k_{pDVC} to 13 p.u. (1.18 times of 11 p.u., which is higher than the GM$=$ 1.13 p.u. of the previous condition $k_{\mathrm{pDVC}} = 11$ p.u.) to make the system unstable. The red dashed Nyquist curves are found in Fig. 9. Both l_{LAAT11} and l_{11} [Fig. 7 (c)] encircle $-1+j0$. Similar to the findings in Section IV-F2, l_{LAAT22} changes dramatically from the condition at $k_{\mathrm{pDVC}} = 11$ p.u., when l_{11} encircles $-1+j0$. This verifies the theory in Section III-B. The time-domain simulation verifies the instability of the closed-loop system, see Fig. 10.

H. Sensitivity Analysis With a Strong-Grid Condition

In this section, we analyze a strong-grid condition with SCR $= 90$ p.u. In the AVC, a voltage control slope equal to 0.03 p.u. is implemented [35], therefore L is derived with an alternative transfer matrix, see Section VII-E. (To satisfy a fast rise-time requirement, k_{iAVC} is chosen as $k_{\mathrm{iAVC}} = 500$ rad/s.) We also assume $u_{\mathrm{pd0}} = 1.1$ p.u. for both conditions. The rest of the control settings are the same as for Section IV-B. The frequency domain and the corresponding time-domain plots[8] are shown in Fig. 11 for the operating point $i_{\mathrm{cq0}} = 0.2$ p.u. (black solid curves) and $i_{\mathrm{cq0}} = -0.2$ p.u. (red dashed curves) respectively. We can see from Fig. 11 (f) that AVC is designed with adequate margins while the DVC is designed more aggressively, see Fig. 11 (a). From $|l_{\mathrm{LAAT12}}|$ in Fig. 11 (b), we find a resonance peak around 10 Hz for both operating conditions. This can be related to the excited time-domain response in Fig. 11 (d) when a step of $\Delta u_{\mathrm{acref}} = 0.02$ p.u. is applied. Similarly, the resonance on Fig. 11 (e) can be correlated with the time-domain response in Fig. 11 (g). With such a strong grid (compared to Section IV-E), the same step change on u_{dcref} causes much smaller variations on u^c_{pdf}, indicating the grid impedance has strong impacts on the interactions from u_{dcref} to u^c_{pdf}. On the other hand, variations on u_{dcf} with the same change on u_{acref} are almost invariant with the grid impedance. In the end, little differences are found in the results between $i_{\mathrm{cq0}} = 0.2$ p.u. and $i_{\mathrm{cq0}} = -0.2$ p.u.

V. Experimental Verifications

In this section, field measurements from a commissioning test of a commercial STATCOM are carried out. The SCR of the grid is approximately 90 p.u. and i_{cq0} is around -0.2 p.u. during the test. Only the step responses are measured to validate a case with the same operating conditions as presented in Section IV-H. Tests are performed with step changes on u_{acref} and u_{dcref}, respectively denoted as Test 1 and Test 2.

The plots for Test 1 to a $\Delta u_{\mathrm{acref}} = 0.02$ p.u. step are shown in Fig. 12 (a) - Fig. 12 (d)[9] with the steady-state condition $i_{\mathrm{cq0}} = -0.248$ p.u. The time-domain comparisons between the LM and the test measurements show good accuracy on the LM for the closed-loop dynamics on u^c_{pdf} and u_{dc}, verifying t_{22} and t_{12}. The Nyquist plots are shown in Fig. 14 (a) based on the conditions of Test 1. It can be seen from l_{LAAT11} and l_{LAAT22} that the DVC and AVC have fairly high gain

[8]With a droop function, the voltage variation after the $\Delta u_{\mathrm{acref}} = 0.02$ p.u step is actually lower than 0.02 p.u.

[9]For a MMC based STATCOM, u_{dc} is computed as the average value of the sum of the capacitor voltages in the three phases.

This article has been accepted for publication in a future issue of this journal, but has not been fully edited. Content may change prior to final publication. Citation information: DOI 10.1109/JESTPE.2020.3024103, IEEE Journal of Emerging and Selected Topics in Power Electronics

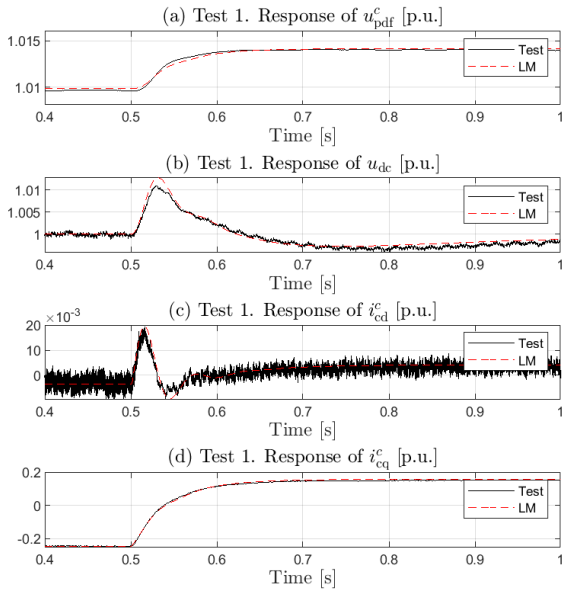

Fig. 12. Responses to a step change of $\Delta u_{\rm acref} = 0.02$ p.u. for the Test 1. Time-domain comparisons between the test (black solid lines) and the LM (red dashed lines). (a) Response of $u^c_{\rm pdf}$. (b) Response of $u_{\rm dc}$. (c) Response of $i^c_{\rm cd}$. (d) Response of $i^c_{\rm cq}$.

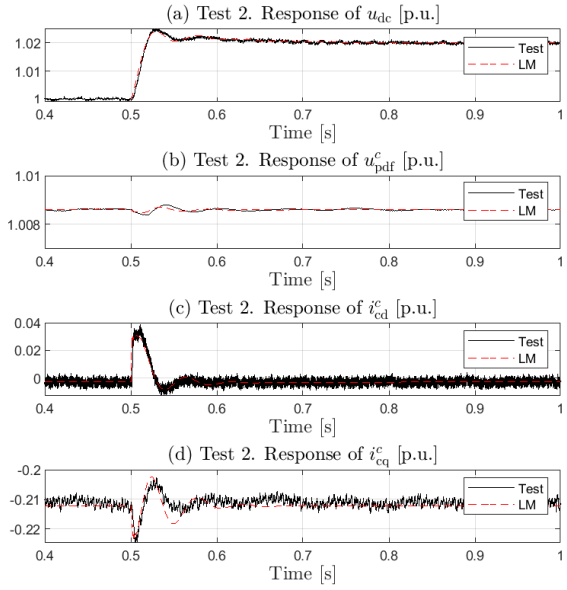

Fig. 13. Responses to a step change of $\Delta u_{\rm dcref} = 0.02$ p.u. for the Test 2. Time-domain comparisons between the test (black solid lines) and the LM (red dashed lines). (a) Response of $u^c_{\rm pdf}$. (b) Response of $u_{\rm dc}$. (c) Response of $i^c_{\rm cd}$. (d) Response of $i^c_{\rm cq}$.

and phase margins for each individual loops under the test conditions. Alike the case shown in Section IV-H, the DVC is designed faster than the AVC [see the rise-time comparison between Fig. 12 (a) and Fig. 13 (a) for the Test 2], the individual closed-loop stability margin for the AVC is higher

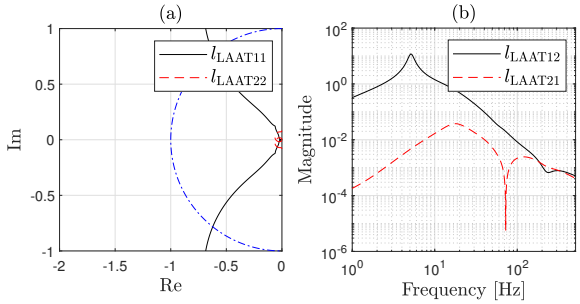

Fig. 14. Test 1. (a) Nyquist plots for $l_{\rm LAAT11}$ and $l_{\rm LAAT22}$. (b) Bode magnitude plots for $l_{\rm LAAT12}$ and $l_{\rm LAAT21}$.

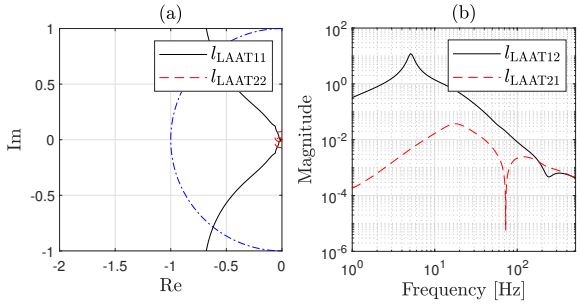

Fig. 15. Test 2. (a) Nyquist plots for $l_{\rm LAAT11}$ and $l_{\rm LAAT22}$. (b) Bode magnitude plots for $l_{\rm LAAT12}$ and $l_{\rm LAAT21}$.

than for the DVC, see Fig. 14 (a) (the relative margins between the DVC and AVC are alike the case shown in Section IV-H). In Fig. 14 (b), $|l_{\rm LAAT12}|$ is higher than $|l_{\rm LAAT21}|$ for almost the whole frequency range, indicating that a perturbation on $u_{\rm acref}$ would cause a larger deviation for the $u_{\rm dc}$ response than the same perturbation on $u_{\rm dcref}$ for the response of $u^c_{\rm pdf}$. For instance, a resonance peak around 5 Hz is observed on $|l_{\rm LAAT12}|$. The excitation of its dynamics can be found in Fig. 12 (b) on the responses of $u_{\rm dc}$ by a step change on $u_{\rm acref}$.

Similarly, Test 2 and the corresponding model validation are shown in Fig. 13, where the plots represent responses to a $\Delta u_{\rm dcref} = 0.02$ p.u. step with $i_{\rm cq0} = -0.213$ p.u. steady-state condition. The LM shows good accuracy to represent the dynamics of $u_{\rm dc}$, as well as the interactions impacts for the $u^c_{\rm pdf}$, having t_{11} and t_{21} verified. Therefore, T is verified by Test 1 and Test 2. The Nyquist and Bode plots for Test 2 are shown in Fig. 15. We can see that due to a similar steady-state condition between the two tests, plots in Fig. 15 are closed to the ones in Fig. 14. Unlike the response shown in Fig. 12 (b), a step on $u_{\rm dcref}$ makes little variations on $u^c_{\rm pdf}$ [Fig. 13 (b)], this can be explained by a relatively small value of $|l_{\rm LAAT21}|$ in Fig. 15 (b). This also verifies the findings in Section IV-H for weaker interactions from $u_{\rm dcref}$ to $u^c_{\rm pdf}$ under stronger-grid conditions. Similarly, a resonance peak around 18 Hz is found in $|l_{\rm LAAT21}|$ in Fig. 15 (b), which can be observed in the time domain [see Fig. 13 (b)].

VI. Conclusions

In this paper, a LAAT stability analysis for grid-connected VSCs is presented. To illustrate the theory, a linearized MIMO

This article has been accepted for publication in a future issue of this journal, but has not been fully edited. Content may change prior to final publication. Citation information: DOI 10.1109/JESTPE.2020.3024103, IEEE Journal of Emerging and Selected Topics in Power Electronics

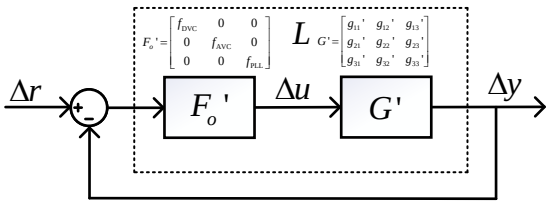

Fig. 16. Schematic of the 3×3 MIMO system structure where PLL is treated as one of the outer-most loops.

model is derived by the cascaded transfer matrices for the stability analysis of the converter–grid interaction. Eventually, the LAAT transfer matrix $L_{\rm LAAT}$ is derived with forward and cross-coupling transfer functions. The design of the outer-loop controllers can thus be evaluated with $L_{\rm LAAT}$. It is shown that, the LAAT stability analysis has close correlations with characteristic loci in the GNC. Moreover, the LAAT analysis allows identifying the stability margins of the DVC and AVC loops individually. Also, the non-diagonal elements of $L_{\rm LAAT}$ can be used to analyze the interactions between the closed loops. Sensitivity analyses with numerical examples verify the effectiveness of the LAAT analysis. Further, the LAAT method is applicable to study $n \times n$ MIMO system in general, regardless of the specific control structure implemented. The PLL dynamics in this paper is embedded inside the plant G. Future research could consider the PLL as one of the three outer closed loops (i.e., DVC, AVC, and PLL) for modeling and analysis. The implementation is illustrated in Fig. 16, where the reference (Δr), input (Δu), and output (feedback) (Δy) are denoted as the general symbols in a control system. $\Delta r = [\Delta u_{\rm dcref}, \Delta u_{\rm acref}, \Delta\theta_{\rm PLLref}]$, $\Delta u = [\Delta i^c_{\rm refd}, \Delta i^c_{\rm refq}, \Delta\omega]$, and $\Delta y = [\Delta u_{\rm dcf}, \Delta u_{\rm pdf}, \Delta\theta]$, $F_o = {\rm diag}(f_{\rm DVC}, f_{\rm AVC}, f_{\rm PLL})$. The modeled system is a 3×3 MIMO. By such implementation, the stability margins for the PLL loops, as well as the interactions between the PLL closed loop and the AVC/DVC loops can be studied. The utilization of the LAAT method for control design of a highly-interacted MIMO is seen as a future research topic. Simulation and measurement results from a converter validate the method.

VII. Appendix

A. Small-Signal Modeling

1) Small-Signal Modeling of the Inner Closed loop: Due to the PLL impact, the change of vector variables from the grid dq frame to the converter dq frame [8] yields the following relations [24]:

$$\Delta u^c_c = \Delta u_c - j u_{\rm c0}\Delta\theta, \tag{21}$$

$$\Delta u^c_p = \Delta u_p - j u_{\rm p0}\Delta\theta, \tag{22}$$

$$\Delta i^c_c = \Delta i_c - j i_{\rm c0}\Delta\theta. \tag{23}$$

The closed-loop transfer function $g_{\rm PLL}$ is formed (from $\Delta u_{\rm cq}$ to $\Delta\theta$) with $\Delta\theta$ fed back as an input to (21) for $\Delta u^c_{\rm c}$

$$\Delta\theta = \underbrace{\frac{h_{\rm PLL} f_{\rm PLL}}{1 + u_{\rm cd0} h_{\rm PLL} f_{\rm PLL}}}_{g_{\rm PLL}} \Delta u_{\rm cq}. \tag{24}$$

To represent PLL dynamics by MIMO formats, substituting (24) into (21) and (24) into (23), respectively, yields

$$\Delta u^c_c = G_{\rm PLL1}\Delta u_c, \quad \Delta i^c_c = \Delta i_c + G_{\rm PLL2}\Delta u_c \tag{25}$$

where $G_{\rm PLL1} = I_2 + G_{\rm PLL0}$, $I_2 = \begin{bmatrix}1 & 0\\ 0 & 1\end{bmatrix}$, $G_{\rm PLL0} = \begin{bmatrix}0 & g_{\rm PLL}u_{\rm cq0}\\ 0 & -g_{\rm PLL}u_{\rm cd0}\end{bmatrix}$, and $G_{\rm PLL2} = \begin{bmatrix}0 & g_{\rm PLL}i_{\rm cq0}\\ 0 & -g_{\rm PLL}i_{\rm cd0}\end{bmatrix}$.

Likewise, the voltage reference vector $\Delta u^c_{\rm ref}$ is transformed to the grid dq frame as $\Delta u_{\rm ref}$ [24]

$$\Delta u_{\rm ref} = \Delta u^c_{\rm ref} + j u_{\rm ref0}\Delta\theta. \tag{26}$$

Substituting (24) into (26) yields

$$\Delta u_{\rm ref} = \Delta u^c_{\rm ref} + G_{\rm PLL3}\Delta u_c \tag{27}$$

where $G_{\rm PLL3} = \begin{bmatrix}0 & -g_{\rm PLL}u_{\rm refq0}\\ 0 & g_{\rm PLL}u_{\rm refd0}\end{bmatrix}$.

For the CC, we construct the following transfer matrices:

$$F_{\rm CC} = \begin{bmatrix}f_{\rm CC} & 0\\ 0 & f_{\rm CC}\end{bmatrix}, \quad H_{\rm uFF} = \begin{bmatrix}h_{\rm uFF} & 0\\ 0 & h_{\rm uFF}\end{bmatrix}. \tag{28}$$

Note that $F_{\rm CC}$ and $H_{\rm iFF}$ (6) form a two degrees-of-freedom control structure [21], see Fig. 3.

2) Small-Signal Modeling of the Outer Closed loop: Using the power balancing rules between the ac and dc side of the converter, $\Delta u_{\rm dc}$ can be computed as

$$\Delta u_{\rm dc} = \frac{u_{\rm cd0}\Delta i_{\rm cd} + u_{\rm cq0}\Delta i_{\rm cq} + i_{\rm cd0}\Delta u_{\rm cd} + i_{\rm cq0}\Delta u_{\rm cq}}{sKC_{\rm dc}u_{\rm dc0}} \tag{29}$$

where $K = 2/3$ is the space-vector scaling constant.

With $\Delta u_{\rm s} = 0$, the following relation is obtained (Fig. 3)

$$\Delta u_{\rm c} = -Z_{\rm gt}\Delta i_c. \tag{30}$$

Merging (29), (30), and $h_{\rm udclp}$ yields

$$\Delta u_{\rm dcf} = G_{\rm o1}\Delta i_c \tag{31}$$

where $G_{\rm o1} = h_{\rm udclp}(u^T_{\rm c0} - i^T_{\rm c0}Z_{\rm gt})/(sC_{\rm dc}u_{\rm dc0}K)$.

Substituting (24) into (22) yields

$$\Delta u^c_{\rm p} = \Delta u_{\rm p} + G_{\rm PLL4}\Delta u_c \tag{32}$$

where $G_{\rm PLL4} = \begin{bmatrix}0 & g_{\rm PLL}u_{\rm pq0}\\ 0 & -g_{\rm PLL}u_{\rm pd0}\end{bmatrix}$, indicates a PLL-related dynamics in G_o.

Similarly, with $\Delta u_{\rm s} = 0$, the following relation is obtained:

$$\Delta u_{\rm p} = -Z_g\Delta i_c. \tag{33}$$

Combining (30), (32), (33), and $h_{\rm uplp}$ yields

$$\Delta u^c_{\rm pdf} = h_{\rm uplp}G_{\rm o2}\Delta i_c \tag{34}$$

where $G_{\rm o2} = [G_{\rm oAVC}(1,1), G_{\rm oAVC}(1,2)]$, $G_{\rm o2AVC} = -Z_g - G_{\rm PLL4}Z_{gt}$.

This article has been accepted for publication in a future issue of this journal, but has not been fully edited. Content may change prior to final publication. Citation information: DOI 10.1109/JESTPE.2020.3024103, IEEE Journal of Emerging and Selected Topics in Power Electronics

B. Comparison With the GNC

In this section, an illustrative example in [12] is used for a comparison between the Nyquist curves respectively plotted by the LAAT and the GNC. The example is described as

$$G = \frac{1}{1.25(s+1)(s+2)}\begin{bmatrix} s-1 & s \\ -6 & s-2 \end{bmatrix}, \quad K = kI_2, \quad (35)$$

and $L = GK$.

First of all, $k = 1$. The Nyquist and Bode magnitude plots are illustrated in Fig. 17 and Fig. 18. The closed loop is stable (none of the Nyquist curves encircles $-1+j0$). From Fig. 18, it can be seen the strong interaction effects in the MIMO by l_{12} and l_{21}. An unstable closed loop is created by $k = 2$. Its Nyquist and Bode magnitude plots are illustrated in Fig. 19 and Fig. 20. It can be seen that both l_{LAAT22} and λ_2 encircles $-1+j0$.

C. Controller Design of Inner Closed Loop

Since this section, we present how to select the parameters for f_{CC}, f_{PLL}, f_{DVC}, and f_{AVC} using SISO modeling with reduced-order transfer functions. The grid is considered to be purely inductive.

1) CC Design: Considering the CC has much higher bandwidth α_{CC} than the PLL α_{PLL} [8], we assume $g_{\mathrm{PLL}} = 0$ for designing the CC. This allows us to design f_{CC} based on the simplified scalar transfer functions t_{CC} for closed-loop dynamics from $\Delta i^c_{\mathrm{refd}}$ to Δi_{cd} or from $\Delta i^c_{\mathrm{refq}}$ to Δi_{cq} (with $g_{\mathrm{PLL}} = 0$, we have $\Delta i_{\mathrm{c}} = \Delta i^c_{\mathrm{c}}$). Considering that k_{iCC} mainly acts on correcting of the steady-state control error, we can further assume that $k_{\mathrm{iCC}} = 0$ when designing k_{pCC} [34]. This yields the following:

$$t_{\mathrm{CC}} = \frac{\alpha_{\mathrm{CC}}}{s + \alpha_{\mathrm{CC}}} \quad (36)$$

where $\alpha_{\mathrm{CC}} = \omega_1 k_{\mathrm{pCC}}/X_{\mathrm{r}}$, k_{pCC} is in p.u. and X_r is the converter phase reactor reactance in p.u. In general, α_{CC} should be high to maintain certain bandwidth separations with other relatively slower closed loops (PLL, DVC and AVC). A typical recommendation is that $\alpha_{\mathrm{CC}} \leq 0.1\omega_s$ [6], where ω_s is the angular sampling frequency. We select $\alpha_{\mathrm{CC}} = 0.05\omega_s$ rad/s. $k_{\mathrm{iCC}} = 10$ rad/s.

2) PLL Design: Considering that h_{PLL} has relative high bandwidth to α_{PLL}, we allow an assumption with $\tau_{\mathrm{PLL}} = 0$. Similar to CC, we thus further assume $k_{\mathrm{iPLL}} = 0$ to facilitate the design. Overall, g_{PLL} is simplified as

$$\frac{k_{\mathrm{pPLL}}}{s + u_{\mathrm{cd0}} k_{\mathrm{pPLL}}}, \quad (37)$$

$\alpha_{\mathrm{PLL}} = k_{\mathrm{pPLL}}$ when $u_{\mathrm{cd0}} \approx 1$. k_{pPLL} thus has rad/s as its unit. Typically $\alpha_{\mathrm{PLL}} \leq 0.1\alpha_{\mathrm{CC}}$ [8]. We choose a more conservative design, i.e., $\alpha_{\mathrm{PLL}} \approx 0.01\alpha_{\mathrm{CC}}$. It is always set for $k_{\mathrm{iPLL}} = 1$ rad/s.

D. Controller Design of Outer Closed Loop

Time-domain specifications for step changes on Δu_{ref} usually include requirements on the rise time of Δu^c_{o}. To correlate such requirement, it is desirable to design the outer-loop controllers using alike closed-loop transfer functions in Section VII-C. However, G is a high-order system which makes it impractical to derive explicit forms of transfer functions for the design. Therefore, a proper order reduction of G is required. Considering that T_i has high bandwidth relative to f_{DVC} and f_{AVC}, we can assume $T_i \approx 1$, giving that $g_{11} = g_{\mathrm{o11}}$ and $g_{22} = g_{\mathrm{o22}}$. Also, we assume that $g_{\mathrm{PLL}} \approx 0$ for the design.

1) DVC Design: The bandwidth of the DVC closed loop α_{DVC} is obtained via $t_{\mathrm{DVC}} = l_{11}/(1 + l_{11})$, a simplified t_{11} from $\Delta u_{\mathrm{dcref}}$ to Δu_{dcf}, where $l_{11} = g_{11} f_{\mathrm{DVC}}$. The explicit form of t_{DVC} yields a third-order system as follows:

$$t_{\mathrm{DVC}} = \frac{\omega_{\mathrm{dceq}} k_{\mathrm{pDVC}}(s + k_{\mathrm{iDVC}})}{\tau_{\mathrm{DVC}} s^3 + s^2 + \omega_{\mathrm{dceq}} k_{\mathrm{pDVC}} s + \omega_{\mathrm{dceq}} k_{\mathrm{pDVC}} k_{\mathrm{iDVC}}} \quad (38)$$

where $\omega_{\mathrm{dceq}} = (u_{\mathrm{cd0}} - \omega_1 L_g i_{cq0})/(C_{\mathrm{dc}} u_{\mathrm{dc0}} K)$.

If we omit the effect of the integral part, i.e., $k_{\mathrm{iDVC}} = 0$, also considering that h_{DVC} has high bandwidth relative to α_{DVC}, (38) can be further simplified ($\tau_{\mathrm{DVC}} = 0$) to its first-order form as

$$t_{\mathrm{DVC}} = \frac{\alpha_{\mathrm{DVC}}}{s + \alpha_{\mathrm{DVC}}} \quad (39)$$

where $\alpha_{\mathrm{DVC}} = \omega_{\mathrm{dceq}} k_{\mathrm{pDVC}}$. k_{pDVC} could be selected such that $\alpha_{\mathrm{DVC}} \leq 0.1\alpha_{\mathrm{CC}}$ [8]. Also, the design should ensure that,

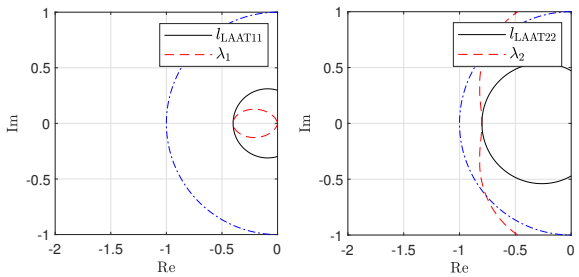

Fig. 17. Nyquist plots for the GNC and LAAT, with $k = 1$.

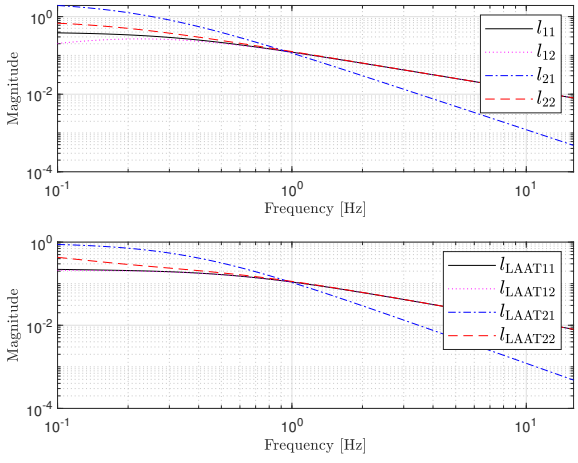

Fig. 18. Bode magnitude plots for the GNC and LAAT, with $k = 1$.

during dynamical conditions, e.g., change of operating points, ac fault, a quick regulation can be achieved for $\Delta u_{\rm dcf} = 0$. Such requirement can be well correlated with the closed-loop dynamics in (39) – we could specify a step response requirement for the regulation of $\Delta u_{\rm dcf}$. Since

$$\mathscr{L}^{-1}\{\frac{(39)}{s}\} = 1 - e^{-\alpha_{\rm DVC}t}, \tag{40}$$

an approximate DVC rise time correlation would be $\tau_{\rm rDVC} \approx 2.2/\alpha_{\rm DVC}$. We set $\tau_{\rm rDVC} = 20$ ms. The integral part is kept slow, i.e., $k_{\rm iDVC} = 10$ rad/s. Furthermore, we notice that for different L_g, $\omega_1 L_g i_{cq0}$ [in $\tau_{\rm dceq}$ of (39)] remains almost unchanged for maximum loading points under various L_g. This means that $\alpha_{\rm DVC}$ should be almost invariant of L_g.

2) AVC Design: Likewise, the AVC bandwidth $\alpha_{\rm AVC}$ can be approximated via $t_{\rm AVC} = l_{22}/(1 + l_{22})$, a simplified t_{22} from $\Delta u_{\rm acref}$ to $\Delta u^c_{\rm pdf}$, where $l_{22} = g_{22} f_{\rm AVC}$. Substituting $f_{\rm AVC}$ by $k_{\rm iAVC}/s$, the explicit form of $t_{\rm AVC}$ yields a second-order system

$$t_{\rm AVC} = \frac{\omega_1 L_g k_{\rm iAVC}}{\tau_{\rm AVC} s^2 + s + \omega_1 L_g k_{\rm iAVC}}. \tag{41}$$

Considering relative high bandwidth of $h_{\rm AVC}$ to $\alpha_{\rm AVC}$, (41) can be simplified with $\tau_{\rm AVC} = 0$ as

$$t_{\rm AVC} = \frac{\alpha_{\rm AVC}}{s + \alpha_{\rm AVC}} \tag{42}$$

where $\alpha_{\rm AVC} = \omega_1 L_{\rm g} k_{\rm iAVC}$. Unlike the design for the other controllers, the AVC design is much related to L_g, see (42). The design is also relevant to the step response requirements [35]. For a specification with the AVC rise time $\tau_{\rm rAVC} = 100$ ms, we have $\alpha_{\rm AVC} \approx 2.2/\tau_{\rm rAVC} = 22$ rad/s. For the design we assume that $k_{\rm iAVC}$ is not required to change adaptively [35] with L_g, then a constant value of $k_{\rm iAVC}$ shall be chosen to fulfill the step-response requirements for $L_g \in [L_{\rm gmin}, L_{\rm gmax}]$, where $L_{\rm gmin}$ is the minimal value of L_g and $L_{\rm gmax}$ denote L_g's maximum value.

E. Derivation of the LAAT Transfer Matrix With Voltage Control Slope Function

When the voltage control slope function is included in the AVC, $e_{\rm AVC} = u_{\rm acref} - u^c_{\rm pdf} - k_{\rm slope} i^c_{\rm pq}$, where $k_{\rm slope}$ is the value for the slope. Therefore, in order to have $u^c_{\rm pdf}$ as the feedback signal to break the AVC loop, an internal feedback loop T_1 is formed [Fig. 21 (a)]. Consequently, $L = G_o T_1$ [Fig. 21 (b)].

$$T_1 = (I_2 + T_i F_o G_{\rm slope} G_{\rm PLL5})^{-1} T_i F_o \tag{43}$$

where $G = \begin{bmatrix} 0 & 0 \\ 0 & k_{\rm slope} \end{bmatrix}$ and $G_{\rm PLL5} = I_2 - G_{\rm PLL2} Z_{\rm gt}$.

REFERENCES

[1] L. Zhang, "Modeling and control of VSC-HVDC links connected to weak AC systems," Ph.D. dissertation, Electrical Machines and Power Electronics, Stockholm, 2010.

[2] C. Buchhagen, C. Rauscher, A. Menze, and J. Jung, "Borwin1 – First experiences with harmonic interactions in converter dominated grids," in *International ETG Congress 2015; Die Energiewende – Blueprints for the new energy age*, Nov. 2015, pp. 1–7.

[3] C. Li, "Unstable operation of photovoltaic inverter from field experiences," *IEEE Trans. Power Deliv.*, vol. 33, no. 2, pp. 1013–1015, Apr. 2018.

[4] C. Zou, H. Rao, S. Xu, Y. Li, W. Li, J. Chen, X. Zhao, Y. Yang, and B. Lei, "Analysis of resonance between a VSC-HVDC converter and the AC grid," *IEEE Trans. Power Electron.*, vol. 33, no. 12, pp. 10 157–10 168, Dec. 2018.

[5] X. Wang and F. Blaabjerg, "Harmonic stability in power electronic-based power systems: Concept, modeling, and analysis," *IEEE Trans Smart Grid*, vol. 10, no. 3, pp. 2858–2870, 2019.

[6] L. Harnefors, X. Wang, A. G. Yepes, and F. Blaabjerg, "Passivity-based stability assessment of grid-connected VSC — An overview," *IEEE Trans. Emerg. Sel. Topics Power Electron.*, vol. 4, no. 1, pp. 116–125, Mar. 2016.

[7] L. Harnefors, R. Finger, X. Wang, H. Bai, and F. Blaabjerg, "VSC input-admittance modeling and analysis above the Nyquist frequency for passivity-based stability assessment," *IEEE Trans. Ind. Electron.*, vol. 64, no. 8, pp. 6362–6370, Aug. 2017.

[8] L. Harnefors, M. Bongiorno, and S. Lundberg, "Input-admittance calculation and shaping for controlled voltage-source converters," *IEEE Trans. Ind. Electron.*, vol. 54, no. 6, pp. 3323–3334, Dec. 2007.

[9] X. Wang, F. Blaabjerg, and W. Wu, "Modeling and analysis of harmonic stability in an AC power-electronics-based power system," *IEEE Trans. Power Electron.*, vol. 29, no. 12, pp. 6421–6432, Dec. 2014.

[10] J. Z. Zhou, H. Ding, S. Fan, Y. Zhang, and A. M. Gole, "Impact of short-circuit ratio and phase-locked-loop parameters on the small-signal behavior of a VSC-HVDC converter," *IEEE Trans. Power Deliv.*, vol. 29, no. 5, pp. 2287–2296, Oct. 2014.

[11] H. Nyquist, "Regeneration theory," *The Bell System Technical Journal*, vol. 11, no. 1, pp. 126–147, Jan. 1932.

[12] A. Macfarlane and I. Postlethwaite, "The generalized Nyquist stability criterion and multivariable root loci," *Int. J. Control*, vol. 25, no. 1, pp. 81–127, 1977.

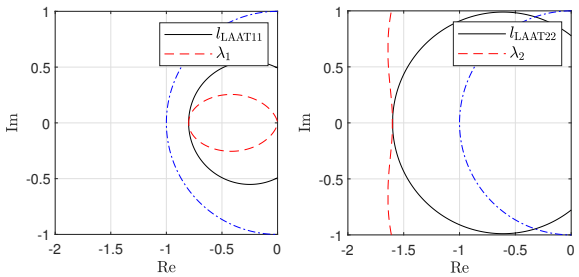

Fig. 19. Nyquist plots for the GNC and LAAT, with $k = 2$.

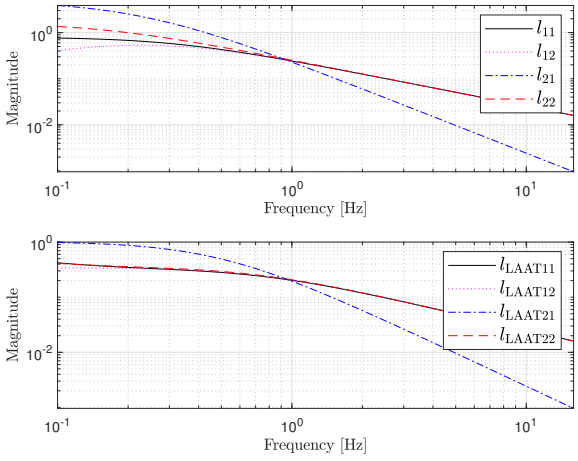

Fig. 20. Bode magnitude plots for the GNC and LAAT, with $k = 2$.

This article has been accepted for publication in a future issue of this journal, but has not been fully edited. Content may change prior to final publication. Citation information: DOI 10.1109/JESTPE.2020.3024103, IEEE Journal of Emerging and Selected Topics in Power Electronics

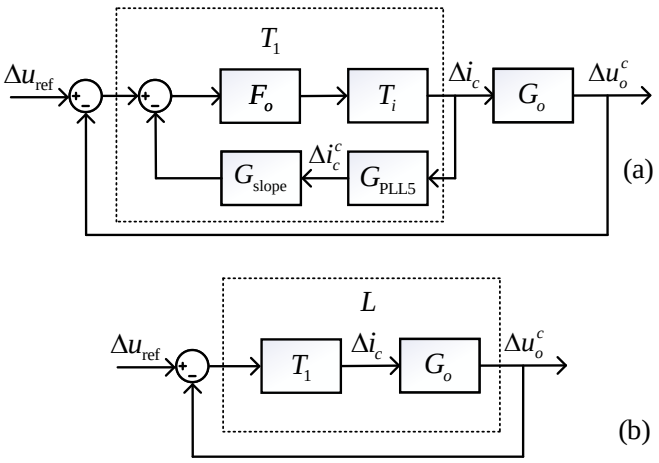

Fig. 21. (a) Schematic of the equivalent MIMO system to Fig. 3. (b) Schematic of the DVC and AVC loops, expressed with l_{11}, l_{12}, l_{21}, and l_{22} in L.

[13] C. Desoer and Yung-Terng Wang, "On the generalized Nyquist stability criterion," *IEEE Trans. Automat. Contr.*, vol. 25, no. 2, pp. 187–196, Apr. 1980.

[14] R. Brockett and C. Byrnes, "Multivariable Nyquist criteria, root loci, and pole placement: A geometric viewpoint," *IEEE Trans. Automat. Contr.*, vol. 26, no. 1, pp. 271–284, Feb. 1981.

[15] A. Macfarlane and J. Belletrutti, "The characteristic locus design method," *Automatica (Oxf)*, vol. 9, no. 5, pp. 575–588, 1973.

[16] J. Maciejowski, *Multivariable Feedback Design*, ser. Electronic systems engineering series. Addison-Wesley, 1989.

[17] J. C. Doyle, K. Glover, P. P. Khargonekar, and B. A. Francis, "State-space solutions to standard H_2 and H_∞ control problems," *IEEE Trans. Automat. Contr.*, vol. 34, no. 8, pp. 831–847, Aug. 1989.

[18] S. Skogestad and M. Morari, "Robust performance of decentralized control systems by independent designs," *Automatica (Oxf)*, vol. 25, no. 1, pp. 119–125, 1989.

[19] D. Q. Mayne, "Sequential design of linear multivariable systems," *Proc. Inst. Electr. Eng.*, vol. 126, no. 6, pp. 568–572, Jun. 1979.

[20] J. Doyle, "Analysis of feedback systems with structured uncertainties." *IET Control. Theory Appl.*, vol. 129, pp. 242–250, 1982.

[21] S. Skogestad and I. Postlethwaite, *Multivariable Feedback Control: Analysis and Design*. John Wiley & Sons, Inc., 2005.

[22] B. Bose, *Power Electronics and Variable Frequency Drives: Technology and Applications*. IEEE Press, 1997.

[23] K. J. Åström and R. M. Murray, *Feedback Systems: An Introduction for Scientists and Engineers*. Princeton University Press, 2008.

[24] H. Zhang, L. Harnefors, X. Wang, H. Gong, and J. Hasler, "Stability analysis of grid-connected voltage-source converters using SISO modeling," *IEEE Trans. Power Electron.*, vol. 34, no. 8, pp. 8104–8117, Aug. 2019.

[25] J. C. Doyle, "Robustness of multiloop linear feedback systems," in *1978 IEEE Conference on Decision and Control including the 17th Symposium on Adaptive Processes*, Jan. 1978, pp. 12–18.

[26] A. Packard, J. Doyle, and G. Balas, "Linear, multivariable robust control with a μ perspective," *J. Dyn. Sys., Meas., Control*, vol. 115, no. 2B, pp. 426–438, Jun. 1993.

[27] J. D. Blight, R. L. Dailey, and D. Gangsaas, "Practical control law design for aircraft using multivariable techniques," *Int. J. Control*, vol. 59, no. 1, pp. 93–137, 1994.

[28] L. Harnefors, A. Antonopoulos, S. Norrga, L. Ängquist, and H.-P. Nee, "Dynamic analysis of modular multilevel converters," *IEEE Trans. Ind. Electron.*, vol. 60, no. 7, pp. 2526–2537, Jul. 2013.

[29] L. Bessegato, K. Ilves, L. Harnefors, and S. Norrga, "Effects of control on the AC-side admittance of a modular multilevel converter," *IEEE Trans. Power Electron.*, vol. 34, no. 8, pp. 7206–7220, 2019.

[30] L. Harnefors, "Modeling of three-phase dynamic systems using complex transfer functions and transfer matrices," *IEEE Trans. Ind. Electron.*, vol. 54, no. 4, pp. 2239–2248, Aug. 2007.

[31] V. Kaura and V. Blasko, "Operation of a phase locked loop system under distorted utility conditions," *IEEE Trans. Ind. Appl.*, vol. 33, no. 1, pp. 58–63, Jan. 1997.

[32] S. Zhou, J. Liu, L. Zhou, and Y. Zhang, "DQ current control of voltage source converters with a decoupling method based on preprocessed reference current feed-forward," *IEEE Trans. Power Electron.*, vol. 32, no. 11, pp. 8904–8921, 2017.

[33] D. Newman, "The analysis of cross-coupling effects on the stability of two-dimensional, orthogonal, feedback control systems," *IEEE Trans. Automat. Contr.*, vol. 5, no. 4, pp. 314–320, Sep. 1960.

[34] L. Harnefors, L. Zhang, and M. Bongiorno, "Frequency-domain passivity-based current controller design," *IET Power Electron.*, vol. 1, no. 4, pp. 455–465, Dec. 2008.

[35] "IEEE guide for specification of transmission static synchronous compensator (STATCOM) systems," *IEEE Std 1052-2018*, pp. 1–115, Apr. 2019.